Efficient and stable operation of nonfullerene organic solar cells

Wang, Yiwen; Han, Jiayin; Cai, Linfeng; Li, Ning; Li, Zhe; Zhu, Fu Rong

Published in:
Journal of Materials Chemistry A

DOI:
10.1039/d0ta08018g

Published: 28/10/2020

Document Version:
Peer reviewed version

Journal of
Materials Chemistry A

Materials for energy and sustainability

Accepted Manuscript

This article can be cited before page numbers have been issued, to do this please use: Y. WANG, J. HAN, L. Cai, N. Li, Z. Li and F. Zhu, *J. Mater. Chem. A*, 2020, DOI: 10.1039/D0TA08018G.

ROYAL SOCIETY OF CHEMISTRY

rsc.li/materials-a

DOI: 10.1039/D0TA08018G

Efficient and Stable Operation of Nonfullerene Organic Solar Cells: Retaining a High Built-in Potential

Yiwen Wang,[1] Jiayin Han,[1] Linfeng Cai,[1] Ning Li,[1] Zhe Li[2] and Furong Zhu*[1]*

[1] Department of Physics, Research Centre of Excellence for Organic Electronics and Institute of Advanced Materials, Hong Kong Baptist University, Kowloon Tong, Hong Kong, China
E-mail: frzhu@hkbu.edu.hk
[2] School of Engineering and Materials Science, Queen Mary University of London, London, United Kingdom
E-mail: zhe.li@qmul.ac.uk

Keywords: stability of nonfullerene organic solar cells, interfacial modification, built-in potential, hole transporting layer, suppression of interfacial reaction

This work reports our research efforts to improve the operational stability of nonfullerene OSCs by retaining a stable and high built-in potential across the bulk heterojunction (BHJ). The stable built-in potential in the OSCs is realized through suppression of the interfacial reaction between the BHJ and poly(3,4-ethylenedioxythiophene)-polystyrene sulfonate (PEDOT:PSS) hole transporting layer (HTL). The impact of interfacial modification, molybdenum oxide (MoO_3) induced oxidation doping of the PEDOT:PSS HTL, on the operational stability of poly[(2,6-(4,8-bis(5-(2-ethylhexyl-3-fluoro)thiophen-2-yl)-benzo[1,2-b:4,5-b']dithiophene))-alt-(5,5-(1',3'-di-2-thienyl-5',7'-bis(2-ethylhexyl)benzo[1',2'-c:4',5'-c'] dithiophene-4,8-dione)] (PBDB-T-2F): 3,9-bis(2-methylene-((3-(1,1-dicyanomethylene)-6,7-difluoro)-indanone))-5,5,11,11-tetrakis(4-hexylphenyl)-dithieno[2,3-d:2',3'-d']-s-indaceno [1,2-b:5,6-

b']dithiophene (IT-4F) nonfullerene OSCs has been analyzed. We found that the MoO_3-induced oxidation doping in PEDOT:PSS can effectively suppress the interfacial chemical reactions between IT-4F and PEDOT:PSS, a recently identified major degradation mechanism in NFA with 2-(3-oxo-2,3-dihydroinden-1-ylidene)malononitrile moieties-based OSCs. Our findings highlight the importance of retaining high built-in potential to mitigate any associated degradation mechanisms, to accompany the rapid advance in the molecular synthesis of NFAs, toward enhanced operational stability of NFA-based OSCs.

1. **Introduction**

The emerging nonfullerene acceptors (NFAs) has strongly motivated the further development of organic solar cells (OSCs), resulting in high-performing single junction OSCs[1] and ternary/tandem OSCs[2–4] with power conversion efficiency (*PCE*) over 17%. Their highly versatile molecular structure has further enabled excellent polymer compatibility with optimal energy levels, resulting in extended light absorption, suppressed recombination and minimal voltage loss. The most promising NFA groups include 3,9-bis(2-methylene-(3-(1,1-dicyanomethylene)-indanone))-5,5,11,11-tetrakis(4-hexylphenyl)-dithieno[2,3-d:2',3'-d']-s-indaceno[1,2-b:5,6-b']dithiophene (ITIC),[5,6] (5Z, 5'Z)-5,5'-((7,7'-(4,4,9,9-tetraoctyl-4,9-dihydro-s-indaceno [1,2-b:5,6-b']dithiophene-2,7-diyl)bis (benzo[c][1,2,5]thiadiazole7,4diyl)) bis(methanylylidene))bis (3-ethyl-2-thioxothiazolidin-4-one) (IDTBR)[7–9] and 3,9-bis(2-methylene- ((3-(1,1-dicyanomethylene)-6,7-difluoro)-indanone))-5,5,11,11-tetrakis(4-hexyl phenyl)-dithieno[2,3-d:2',3'-d']-s-indaceno[1,2-b:5,6-b']dithiophene (Y6) families.[1,10,11] Acceptor-donor-acceptor (A-D-A) is a popular molecular structure. It has been widely used in a large variety of NFAs to achieve promising photovoltaic properties. This is because the push-

View Article Online
DOI: 10.1039/D0TA08018G

pull A-D-A structure broadens the light absorption in NFAs through the formation of an intramolecular charge transfer effect.[6] For example, ITIC NFA, which is made up of one center analogue-indacenodithieno[3,2-b]thiophene (IDTT) and two 2-(3-oxo-2,3-dihydroinden-1-ylidene)malononitrile (INCN) groups, the intramolecular charge transfer occurs between the IDTT and INCN. This intramolecular charge transfer effect can be modulated by introducing electron pushing or withdrawing groups forming the ITIC derivatives, such as IT-4F, fluorine atoms are introduced into INCN moieties.[5]

Despite the rapid advances in the molecular design of NFAs enabling high device performance, substantial improvement in operational stability of nonfullerene OSCs is needed if organic photovoltaics is to become a viable option for commercialization. A fundamental understanding of the degradation mechanisms is essential to the development of any new design rules to achieve superior operational stability of NFA-based OSCs. The performance and the stability of the OSCs also closely associate with the electronic properties of the hole transporting layer (HTL) or electron transporting layer (ETL). The insert of a buffer layer with suitable energy levels and interfacial electronic properties is not only able to significantly improve charge collection by eliminating excessive recombination and defects (e.g., interfacial trap states), but also has a major impact on operational stability of OSCs.[12–14] For example, the optimization of the PEDOT:PSS interlayer can result in an improved operational stability of the OSCs in air due to the neutralization of its acidic nature.[15,16] Among the commonly used interlayer materials for OSCs, the conducting conjugated PEDOT:PSS is widely utilized HTL in OSCs over the past years, including the recent, wide application in state-of-the-art nonfullerene OSCs,[1,11] due to their high optical transparency and electrical conductivity,

suitable work function, ease processing and good compatibility with OSC fabrication. However, several major degradation mechanisms in OSCs are closely associated with the acidic and hydrophilic nature of the PEDOT:PSS, such as corrosion of the indium-tin-oxide (ITO) electrode and degradation due to humidity exposure.[17–20] The impact of PEDOT:PSS HTL on the stability of the photoactive layer, e.g., due to the interfacial chemical reactions, is less understood, in particular the extensively used PEDOT:PSS HTL in NFA-based OSCs. We have recently shown that PEDOT structures that are positively charged in the PEDOT:PSS HTL could react with electron-accepting INCN moieties in ITIC acceptor, causing an undesired decrease in built-in potential (V_0) across the BHJ, and thereby affect the operational stability of the nonfullerene OSCs.[21-23] It becomes clear that the interfacial engineering is an effective approach to mitigate the interfacial reaction, and thereby improving the operational stability of nonfullerene OSCs.

In this work, we report our effort to develop an effective interfacial engineering approach to improve the operational stability of NFA-based OSCs without compromising device performance. The chemical reaction between the PEDOT chains and INCN moieties, a key degradation mechanism identified at the PBDB-T-2F:IT-4F/PEDOT:PSS interface in OSCs can be suppressed using a hybrid MoO_3-PEDOT:PSS HTL, prepared using a precursor solution with a volume ratio of MoO_3 to PEDOT:PSS of 1:1. The use of a hybrid MoO_3-PEDOT:PSS HTL also helps to enhance the built-in potential in the OSCs. A high and stable V_0 is essential to efficient charge transport, efficient charge extraction, and stable operation of the OSCs. As a result, OSCs with a hybrid MoO_3-PEDOT:PSS HTL exhibit a significantly enhanced operational stability as compared to the reference cells with a pristine PEDOT:PSS HTL,

View Article Online
DOI: 10.1039/D0TA08018G

without compromising the cell performance. Our approach demonstrates the importance of interfacial control on improving the operational stability of OSCs and highlight the urgency to develop novel HTLs that are compatible for various types of nonfullerene OSCs.

2. Device Performance

Figure 1a shows the current density–voltage (*J–V*) characteristics of OSCs with a hybrid MoO_3-PEDOT:PSS HTL, prepared using the MoO_3-PEDOT:PSS precursor solutions with different volume ratios of MoO_3 solution to PEDOT:PSS, and a control device with a pristine PEDOT:PSS HTL. A performance summary of the PBDB-T-2F:IT-4F-based OSCs made with different HTLs of PEDOT:PSS, MoO_3, and MoO_3-PEDOT:PSS is listed in Supporting Information (SI) **Table S1**. All the OSCs studied in this work were encapsulated in the glovebox, with O_2 and H_2O levels < 0.1 ppm, before taking out for stability tests and analyses. The cell results presented in the work are averaged from more than 30 NFA-OSCs fabricated using the same conditions. The aging tests would help us to understand the degradation pathways of the NFA-based OSCs through analyses of the built-in potential across the binary PBDB-T-2F:IT-4F BHJ and maintaining a high built-in potential for enhancing the operational stability of NFA-based OSCs. The use of the hybrid MoO_3-PEDOT:PSS HTL prepared using a MoO_3-PEDOT:PSS precursor solution having a volume ratio of MoO_3 solution to PEDOT:PSS of 1:1 leads to the best cell performance. The OSCs with an optimal hybrid MoO_3-PEDOT:PSS HTL possess an average *PCE* of 13.19%, an average short circuit current density (J_{SC}) of 21.71 mA/cm^2, an average open circuit voltage (V_{OC}) of 0.86 V, and an average fill factor (*FF*) of 70.56%. They are similar to the performance of the control OSCs with a

comparable *PCE* of 13.41%, a J_{SC} of 23.91 mA/cm^2, a V_{OC} of 0.86 V, and an *FF* of 65.30%. The OSCs with a MoO_3-PEDOT:PSS HTL and control cell had the similar *J–V* characteristics, suggesting that the use of a hybrid MoO_3-PEDOT:PSS HTL does not significantly affect the initial efficiency of the OSCs.

In this work, we have selected the optimal OSCs with different HTLs for aging tests and comparison studies. The optimized MoO_3-PEDOT:PSS-based OSCs had a 110 nm thick optimal BHJ, and the control cells had a 130 nm thick optimal BHJ. The slightly lower J_{SC} of the OSCs with a hybrid HTL, in comparison to that of a control cell, is related to the thinner BHJ used in the devices. The OSCs with a hybrid HTL possess a high built-in potential and charge extraction efficiency as compared to that of the control OSC, as seen in **Figure S1**. The poorer charge extraction in the control cell would lead to an undesired build-up of space charges near the vicinity of the electrodes, allowing the charge recombination to take place, and thereby leading to a slight decrease in the *FF* of the control cell. **Figure 1b** shows the normalized *PCE* of the OSCs as a function of the aging time. The OSCs were encapsulated using a glass cap with edges sealed using a UV cured epoxy in the glovebox with O_2 and H_2O levels <0.1 ppm before taking out for the characterization and aging test in air. The encapsulated OSCs were kept in the dry box before and after the characterization for shelf stability analysis. The deterioration in the performance of the OSCs with a pristine HTL and a hybrid MoO3-PEDOT:PSS HTL can then be analyzed with the minimum inference caused by the possible encroachment of the oxygen and moisture.

The *PCE* of the OSCs with a MoO_3-PEDOT:PSS HTL reduced to half of its initial efficiency

after an 80-day aging test. However, the efficiency of a control OSC dropped by 50% only after a period of 15 days. The operational stability of OSCs with a MoO_3-PEDOT:PSS HTL is more than five times longer than that of the control cells. The fast degradation in control OSCs is mainly due to a 40% decrease in V_{OC} during the aging test. *FF* of the control cell also showed a dramatic drop of around 31%, along with an 11% decrease in J_{SC}, leading to an overall 63% decrease in *PCE*. The normalized V_{OC}, J_{SC} and *FF* as a function the aging time are shown in **Figure S2**. The deterioration in the stability of the nonfullerene OSCs is related to a continuous vertical stratification of PBDB-T-2F and IT-4F in BHJ during the aging period, intrinsic deterioration of the organic functional materials due to the encroachment of oxygen and moisture encroachment, and the interfacial chemical reaction at the organic/contact interfaces etc. In this work, it shows that the use of the hybrid MoO_3-PEDOT:PSS HTL has the advantage to improve the efficiency and the stability of the OSCs as compared to the control cell. Although an initial device degradation is still observed, the advantage of incorporating a hybrid MoO_3-PEDOT:PSS HTL in the PBDB-T-2F:IT-4F OSCs has been clearly demonstrated.

3. Effect of Built-in Potential on Stability of OSCs

The built-in potential across the PBDB-T-2F:IT-4F BHJ and its effect on the operational stability of the OSCs were analyzed using the transient photocurrent (TPC) measurements.[21,22,23] TPC characteristics measured for OSCs made with a MoO_3-PEDOT:PSS HTL and a pristine PEDOT:PSS HTL, operated under different offset biases, are plotted in **Figure 2 a** and **b**. For a control cell, an offset bias of 0.96 V was needed to compensate the transient photocurrent, suggesting a control cell has a V_0 of 0.96 V. While a higher offset bias of 1.06 V was required to compensate the transient photocurrent in the TPC measured for a OSC with an optimal hybrid MoO_3-PEDOT:PSS HTL, implying a higher a V_0

View Article Online
DOI: 10.1039/D0TA08018G

of 1.06 V. The results show that the OSCs with a MoO_3-PEDOT:PSS HTL has a higher V_0 than that in the control OSCs. Higher V_0 in OSCs with a MoO_3-PEDOT:PSS HTL helps efficient charge transport and extraction through suppression of bimolecular recombination in PBDB-T-2F:IT-4F-based OSCs.

V_0 in OSCs, having different HTLs, as a function of the aging time was examined. The results are presented in **Figure 2 c**. The evolution of the V_0 as a function of the aging time agrees well with the variation of the V_{OC} as a function of the aging time, as shown in **Figure S2 b**. A fast drop in V_0 is observed in the OSCs during the first 20 days of the aging test following with a relatively steadily built-in potential. A 35% decrease in V_0 was observed for the OSCs with a hybrid MoO_3-PEDOT:PSS HTL after an 80-day aging test. However, there is a nearly 50% decrease in V_0 in the control devices during the aging test. It reveals that the OSCs with a hybrid MoO_3-PEDOT:PSS HTL have a higher and more stable V_0 across the BHJ as compared to that of the control cells. A high and stable V_0 is a prerequisite for efficient and stable operation of the OSCs, facilitating an efficient charge transport through reduced charge recombination in OSCs.[23]

To investigate the charge transport behavior in OSCs with different HTLs, the charge extraction probability (P) of the OSCs as a function of the aging time was examined, the results are shown in **Figure 2 d**. The charge extraction probability P is defined by **Equation 1**:

$$P = \frac{J_{ph,0}}{J_{sat}}, \quad (1)$$

where $J_{ph,0}$ is the photocurrent density of the cells without bias, J_{sat} is the saturated

photocurrent.[22,24] The photocurrent density (J_{ph}) – effective voltage (V_{eff}) (J_{ph}– V_{eff}) characteristics of as-prepared OSCs with different HTLs are shown in **Figure S1**. The charge extraction probability of the as-prepared OSCs with a MoO_3-PEDOT:PSS HTL is 0.95 while *P* of the as-prepared control cell is 0.92. After an 80-day aging test, the charge extraction probability of the OSCs with a hybrid MoO_3-PEDOT:PSS HTL decreases to 0.92, remaining almost 97% of its initial value. The charge extraction probability of the control OSCs drops to 0.86, remaining of 93% of its original value. The charge extraction probability of the control cells decreases faster than that of the OSCs with a hybrid MoO_3-PEDOT:PSS HTL. The results illustrate that the use of a hybrid MoO_3-PEDOT:PSS HTL increases and stabilizes V_0 across the PBDB-T-2F:IT-4F BHJ, enhances the charge dissociation probability in OSCs, and also results in an efficient charge transport process during the aging test.

X-ray photoelectron spectroscopy (XPS) and Raman spectroscopy measurements were used to analyze the variation of the V_0 in PBDB-T-2F:IT-4F-based OSCs with different HTLs. The vertical stratification of PBDB-T-2F and IT-4F in the BHJ was examined by analyzing the change in the relative elemental composition ratio of PBDB-T-2F to IT-4F on the top and bottom surfaces of the binary PBDB-T-2F:IT-4F blend layer using XPS measurements. A substrate dependent vertical phase separation between the polymer and acceptor in the BHJ has been reported for some blend systems, we found that such substrate dependence is relatively weak for ITIC family-based binary blends. For example, we found that ZnO, PEDOT:PSS, and glass substrate surface shows similar effect on vertical phase separation of ITIC-based blend film in our work. [21,22] The area ratios of N_{1S} XPS peak to S_{2P} XPS peak, measured for the top surfaces of the binary PBDB-T:NFA blend layers having INCN groups in NFA, e.g., ITIC,

View Article Online
DOI: 10.1039/D0TA08018G

formed on different substrates are listed **Table S2**. The results suggest that the composition ratios of the polymer to INCN-containing NFA families measured for the top surfaces of the binary blend layers formed on different substrates of Si, PEDOT:PSS, MoO_3 and ZnO substrates is consistently lower than that measured at the bottom surface (~0.262), implying a similar inhomogeneous vertical stratification in the blend films, that is relatively insensitive to the bottom substrate. For this reason, we have used PBDB-T-2F:IT-4F/Si samples for the XPS measurement, due to the ease process for sample preparation. The wide scan XPS spectra measured for a pure PBDB-T-2F film and a pure IT-4F film deposited on Si substrates are shown in **Figure 3 a**. S_{2p}, S_{2s}, C1s, O1s, and F_{1s} XPS peaks are seen in the XPS spectra measured for the PBDB-T-2F film and IT-4F film, but N_{1s} XPS peak is only seen in IT-4F film. Thus, the changes in the ratios of the of N_{1s} XPS peak area to that of F_{1s} (N_{1s}/F_{1s}), and N_{1s} XPS peak area to that of S_{2p} (N_{1s}/S_{2p}) at the bottom and top surfaces of the active layer reflect the inhomogeneous in the vertical distribution of PBDB-T-2F and IT-4F in the binary blend layer. The wide XPS scan, N_{1s}, F_{1s}, and S_{2p} XPS spectra measured for the bottom and top surfaces of the binary PBDB-T-2F:IT-4F blend layer are shown in **Figure 3 b**. The elements associated with the PBDB-T-2F and IT-4F in the blend layer are detected. The ratios of N_{1s}/F_{1s} and N_{1s}/S_{2p} obtained for the top and bottom surfaces of the blend layer as a function of the aging time are shown in **Figure 3 c** and **d**. The ratios of N_{1s}/F_{1s} and N_{1s}/S_{2p} at bottom surface of the blend layer are higher than those at the top surface of the as-prepared BHJ samples, illustrating that the vertical distribution of IT-4F in the BHJ layer is not uniform. There is an IT-4F-rich region towards the bottom surface of the blend layer. It shows that the ratios of N_{1s}/F_{1s} and N_{1s}/S_{2p} at the bottom surface of the blend layer increase with the aging time, and those at the top surface

View Article Online
DOI: 10.1039/D0TA08018G

decline with the aging time. These results prove that an inhomogeneous vertical stratification occurs continuously in the BHJ during the aging period, resulting in an IT-4F-rich region formed gradually towards the bottom surface and a PBDB-T-2F-rich region towards the top surface in the BHJ layer during the aging period.

The possible chemical reaction between the MoO_3-PEDOT:PSS HTL and IT-4F nonfullerene acceptor at the HTL/BHJ interface in the PBDB-T-2F:IT-4F-based OSCs was analyzed using Raman spectroscopy measurements. Raman spectra of IT-4F deposited on a hybrid MoO_3-PEDOT:PSS layer and a pristine PEDOT:PSS layer are shown in **Figure 4 a**. Raman spectra of a pristine PEDOT:PSS film and a hybrid MoO_3-PEDOT:PSS film were also measured for comparison studies. As shown in **Figure 4 a**, the PEDOT quinoidal structure has a characteristic peak at the wavenumber of 1451 cm^{-1}. An obvious peak shift of 6 cm^{-1} in the Raman spectrum of PEDOT:PSS overlaid with a thin IT-4F layer, was observed. The charge transfer between INCN moieties and positively charged PEDOT components is likely to take place because of the interaction between PEDOT and INCN at the PEDOT:PSS/IT-4F interface. The shift in the characteristic Raman peak observed for the bilayer PEDOT:PSS/IT-4F sample reveals an obvious change in the quinoidal configuration in PEDOT. However, no obvious shift in peak position is observed for the bilayer MoO_3-PEDOT:PSS/IT-4F sample. It implies that the interaction between the PEDOT units and INCN moieties at the PEDOT:PSS/IT-4F interface is averted at the MoO_3-PEDOT:PSS/IT-4F interface, suggesting that a hybrid MoO_3-PEDOT:PSS HTL favors a stable and high V_0 across the BHJ region, and thereby improving the operational stability of the nonfullerene OSCs.

4. Electronic Properties of the Hybrid MoO_3-PEDOT:PSS HTL

In a previous work, we found that MoO_3-induced oxidation doping in PEDOT:PSS promotes the networking between the PEDOT units, resulting in an increase in the electric conductivity and the work function of the PEDOT:PSS layer.[25] The MoO_3-induced oxidation doping in PEDOT:PSS and the associated chemical reaction through charge transfer between MoO_3 and PEDOT:PSS in the hybrid HTL were investigated using the XPS and UV-visible-near infrared (NIR) absorption measurements.

The Mo_{3d} XPS spectra measured for the MoO_3-PEDOT:PSS and MoO_3 layers are presented in **Figure 5 a** and **b**. The valence electronic states of Mo atoms in the MoO_3 layer were studied. XPS measured for Mo^{6+} with spectra peaks at 236.02 eV and 232.82 eV were simulated. While the XPS spectra measured for Mo^{5+} with peaks locating at 235.02 eV and 231.92 eV are observed in the MoO_3-PEDOT:PSS layer. The appearance of Mo^{5+} in MoO_3-PEDOT:PSS film indicates the oxidation of PEDOT:PSS, caused by the charge transfer between MoO_3 and PEDOT chains. The charge transfer between MoO_3 and PEDOT suppresses the interfacial reaction between PEDOT:PSS and IT-4F at the MoO_3-PEDOT:PSS/IT-4F interface.

The interaction between PEDOT:PSS and MoO_3 in the MoO_3-PEDOT:PSS HTL is further examined using the UV-visible-NIR absorption measurements. A pristine PEDOT:PSS film and a hybrid MoO_3-PEDOT:PSS film with the same thickness of 150 nm, and a 30 nm thick pure MoO_3 film were deposited on quartz substrates for the absorption measurements. The absorption of the PEDOT:PSS layer is associated with the π-π□ transition in the PEDOT units in the PEDOT:PSS layer. In comparison to the pristine PEDOT:PSS film, an obvious absorption enhancement in the MoO_3-PEDOT:PSS film over the wavelength of > 462 nm

View Article Online
DOI: 10.1039/D0TA08018G

(visible and NIR region) is observed, as shown in **Figure 5 c**. The increase in the absorption over the long wavelength range is not attributed to the MoO_3 addition since a pristine MoO_3 layer has a very weak absorption in the long wavelength range. The enhancement in the absorption of the hybrid MoO_3-PEDOT:PSS HTL over the long wavelength region suggests that the change in the configuration of the PEDOT units is due to the MoO_3-induced oxidation doping of PEDOT:PSS.[25,26] The MoO_3-induced oxidation doping of PEDOT:PSS relaxes the charge transfer between and the PEDOT units and INCN moieties at the HTL/BHJ interface due to the charge transfer between the PEDOT and MoO_3 in the hybrid HTL, and thereby prolongs the shelf-life of PBDB-T-2F:IT-4F-based OSCs as shown in **Figure 2** and **Figure 4**.

The electronic properties of a hybrid MoO_3-PEDOT:PSS HTL and a pristine PEDOT:PSS HTL were analyzed using the XPS measurements, the XPS results are shown in **Figure S3**. The XPS S_{2p} peak observed over the binding energy range from 166 to 172 eV is attributed to the contribution of the S atoms in PSS, while the XPS S_{2p} peak over the binding energy range from 162 to 166 eV is associated with the contribution of the S atoms in the PEDOT structure. The ratio of S_{2p} (PSS) XPS peak area and to that of the S_{2p} (PEDOT) was calculated to aid in further analyses on the interaction between MoO_3 and PEDOT. The ratio of PSS to PEDOT in the pristine PEDOT:PSS layer was 7.92, while a lower ratio of PSS to PEDOT of 5.47 was obtained for the MoO_3-PEDOT:PSS HTL. Since MoO_3 solution was dissolved in isopropyl alcohol (IPA) solvent, the S_{2p} XPS spectra measured for IPA-PEDOT:PSS (1:1) was also plotted for comparison as shown in **Figure S3 c**. The calculated S_{2p} (PSS) to S_{2p} (PEDOT) ratio of IPA-PEDOT:PSS (1:1) was 5.05, very close to the value obtained for the MoO_3-PEDOT:PSS HTL. The MoO_3 solution was formulated by dissolving the MoO_3 powders in IPA solvent. IPA in

the MoO_3-PEDOT:PSS precursor solution has the effect on partial removal PSS from PEDOT:PSS, thereby leading to a decrease in the PSS/PEDOT ratio. The removal of the PSS in PEDOT:PSS results in an increase in the conductivity through improved connection between the PEDOT units in the PEDOT:PSS film.[25,26]

Work function of the hybrid MoO_3-PEDOT:PSS HTL was analyzed by ultraviolet photoelectron spectroscopy (UPS) measurements. UPS spectra measured for the MoO_3-PEDOT:PSS layer and pristine PEDOT:PSS are shown in **Figure S4**. The locations of secondary electron cut-off in UPS spectra measured for a MoO_3-PEDOT:PSS layer and a pristine PEDOT:PSS layer (inset in **Figure S4**) are 16.00 eV and 16.03 eV, having a corresponding a work function of 5.22 eV and 5.19 eV respectively. In comparison to a pristine PEDOT:PSS film, a 0.03 eV increase in the work function of the MoO_3-PEDOT:PSS layer was observed as compared to that measured for a pristine PEDOT:PSS film. An increase in the work function of the MoO_3-PEDOT:PSS HTL helps to reduce the interfacial barrier at the HTL/BHJ interface, which is favorable for charge extraction at the anode/HTL interface in OSCs.

The UPS results support the discussion made with the TPC measurements. There are two reasons result in the OSCs with a hybrid MoO_3-PEDOT:PSS HTL having a higher built-in potential as compared to that in a control cell: (1) the UPS measurement reveal that the hybrid MoO_3-PEDOT:PSS HTL has a higher work function of 5.22 eV as compared to that of 5.19 eV measured for the PEDOT:PSS HTL, as shown in **Figure S4**. Since a 20 nm thick ZnO ETL is used in the OSCs with different HTLs, the OSCs with a pair of a hybrid MoO_3-PEDOT:PSS

View Article Online
DOI: 10.1039/D0TA08018G

HTL and a ZnO ETL would possess a greater different in energy levels between the HTL and ETL, thereby a higher effective internal potential would be expected in the OSCs with a hybrid MoO_3-PEDOT:PSS HTL. (2) The PBDB-T-2F:IT-4F/MoO_3-PEDOT:PSS interface in the OSCs with a hybrid HTL is chemically more stable as compared to that at the PBDB-T-2F:IT-4F/PEDOT:PSS interface in the control OSC, therefore the use of a hybrid MoO_3-PEDOT:PSS HTL helps to retain a higher V_0 across the BHJ, favoring for the efficient and stable operation of the OSCs.

5. Morphology Characterization

The effect of using a MoO_3-PEDOT:PSS HTL on the morphology of the binary PBDB-T-2F:IT-4F blend layer was analyzed using the grazing-incidence wide-angle X-ray scattering (GIWAXS) measurements. The two-dimensional (2D) GIWAXS patterns obtained for the pristine PBDB-T-2F and pristine IT-4F films are shown in **Figure S5**, revealing the obvious (010) peaks in both out of plane direction and in-plane direction. This suggests that the molecular packing of both donor and acceptor molecules has a preferred face-on orientation. The face-on orientation facilitates charge transport in the vertical direction, e.g., in OSCs. **Figure 6 a-f** show GIWAXS two-dimensional patterns of PBDB-T-2F:IT-4F BHJ film deposited on a MoO_3-PEDOT:PSS layer and a pristine PEDOT:PSS film measured during different periods of the aging test. The corresponding one-dimensional line cuts in the out of plane and the in-plane are displayed in **Figure 6 a'- f'**. The parameters are summarized in **Table S3**. The (100) peaks seen in **Figure 6** are associated with the lamellar structure in the neat PBDB-T-2F film. The (100) peaks center at 0.33 $Å^{-1}$ remain stable during the aging test

View Article Online
DOI: 10.1039/D0TA08018G

for BHJ films formed on two different HTL, indicating that no observable change in the lamellar packing is observed in the PBDB-T-2F:IT-4F blend layers formed on the PEDOT:PSS and MoO_3-PEDOT:PSS HTLs.

The π-π stacking peak of (010) locates at 1.61$Å^{-1}$ initially. For PBDB-T-2F:IT-4F BHJ film formed on the MoO_3-PEDOT:PSS, (010) peak shifts to 1.62 $Å^{-1}$ after 14-day degradation and then shifts back to 1.61 $Å^{-1}$ after another 5 days. For the control samples formed on a pristine PEDOT:PSS film, the (010) peak remains at 1.61 $Å^{-1}$ after a 14-day aging test, and then increases to 1.63 $Å^{-1}$ after a 19-day aging test. According to the Scherer equation, the corresponding d-spacing and coherence length of the as-prepared blend film deposited on the hybrid MoO_3-PEDOT:PSS layer are around 3.90 Å and 9.40 Å respectively. The d-spacing and coherence length of as-prepared blend film deposited on the pristine PEDOT:PSS are around 3.89 Å and 9.31 Å respectively. The d-spacing of PBDB-T-2F:IT-4F blend layer formed on different HTLs show a similar value, but the coherence length of blend film deposited on the MoO_3-PEDOT:PSS surface is larger than that of the blend film on the pristine PEDOT:PSS. After a 19-day aging test, the d-spacing of blend film deposited on the MoO_3-PEDOT:PSS layer remains at 3.90 Å, but its coherence length increases to 9.44 Å. For the binary blend layer formed on the pristine PEDOT:PSS layer, its d-spacing decreases to 3.84 Å while its coherence length also reduces to 9.22 Å.

By applying a MoO_3-PEDOT:PSS HTL, the coherence length of the blend film is enlarged, the enlarged coherence length is favorable for charge transport and the suppression of bimolecular recombination. The blend film formed on the MoO_3-PEDOT:PSS surface also shows a stable

View Article Online
DOI: 10.1039/D0TA08018G

π-π stacking behavior during the aging test with the unchanged d-space value, agreeing well with the results of Raman spectroscopy. The interfacial reaction between PEDOT:PSS and IT-4F at the HTL/BHJ interface in OSCs with a pristine PEDOT:PSS HTL can be hindered by incorporating a hybrid MoO_3-PEDOT:PSS HTL, and thereby prolonging the lifetime of the PBDB-T-2F:IT-4F-based OSCs.

Apart from the suppression of the interfacial reaction at the PEDOT:PSS/BHJ interface, the use of the MoO_3-PEDOT:PSS HTL aids in further advantages on the air stability of the OSCs and hole mobility in the HTL. It was reported that the fullerene-based OSCs with a MoO_3-PEDOT:PSS HTL had a considerab improvement in the air stability as compared to the ones with a pristine PEDOT:PSS HTL. This was due to the use of a hybrid MoO_3-PEDOT:PSS HTL with a low hygroscopicity as compared to that of a hygroscopic PEDOT:PSS HTL.[26] The presence of the defects in the MoO_3, e.g., oxygen vacancies, may act as the additional pathway for hole extraction in the OSCs.[27] The effect of the presence of the MoO_3 defects on the hole mobility (μ_h) of the PEDOT:PSS HTL with an additional of the inorganic MoO_3 nanoparticles was analyzed using the space-charge limited current–voltage (SCLC) technique. The hole-only devices with the layer configurations of ITO/PEDOT:PSS/Au and ITO/MoO_3-PEDOT:PSS/Au were prepared for the SCLC measurements. The $J^{0.5}$–V characteristics measured for ITO/PEDOT:PSS/Au and ITO/MoO_3-PEDOT:PSS/Au devices, operated under the forward biases, are plotted in **Figure S6**. We found that the hybrid MoO_3-PEDOT:PSS layer possesses a higher μ_h of 2.61×10^{-5} $cm^2/V\cdot s$, which is >30% higher than that of the pristine PEDOT:PSS film (1.96×10^{-5} $cm^2/V\cdot s$). The use of the hybrid HTL favors the charge extraction in the OSCs due to the improvement in its hole mobility. The SCLC results suggest that the presence of the inorganic MoO_3 nanoparticles in the hybrid HTL also benefits to the hole extraction, and thereby leading to the efficient operation of the OSCs.

In this work we have demonstrated that interfacial modification can be a powerful device engineering strategy to achieve significantly enhanced operational stability of the nonfullerene OSCs. While the rapid advances in the molecular design of high performance NFAs and their matching donor polymers have enabled OSCs with a PCE in exceeding 18%,[1] yet there are very few reports that employ interfacial modification to enhance the efficiency and operational stability of the nonfullerene OSCs. In particular, PEDOT:PSS, a widely used HTL for OSCs, is generally stable with fullerene blend system due to the minimal interfacial chemical reactions. However, this may not be true for NFA-based OSCs as shown in this work, largely due to the structural diversity of NFAs, which may facilitate new chemical reactions, hence the additional device degradation pathways. We have previously found that PEDOT:PSS is highly reactive to the INCN moieties in ITIC acceptor via an intramolecular charge transfer effect, causing an undesired degradation in ITIC-based OSCs. In this work we have identified that the same interfacial reaction can occur between PEDOT:PSS and IT-4F due to a similar molecular structure of IT-4F to ITIC. It thus appears that PEDOT:PSS may react with a range of emerging NFAs which employ a similar structure to ITIC, especially the INCN groups, including the highly successful ITIC and Y6 families. The results presented in this work highlight the importance of retaining a high built-in potential through designing compatible HTLs and ETLs for enhancing the operational stability of the emerging NFA-based OSCs. Further investigations on the impact of interfacial engineering upon the operational stability of nonfullerene OSCs under real life conditions, e.g., light soaking and thermal stress is currently underway.

6. Conclusions

View Article Online
DOI: 10.1039/D0TA08018G

In this work, we have systematically analyzed the impact of retaining a high built-in potential, through interfacial modification, on the operational stability of the PBDB-T-2F:IT-4F-based OSCs. It is clear that the use of an optimal hybrid MoO_3-PEDOT:PSS HTL results in a substantial enhancement in the operational stability of the nonfullerene OSCs. The MoO_3-induced oxidation of the PEDOT:PSS, due to the charge transfer between the PEDOT and MoO_3 in the hybrid MoO_3-PEDOT:PSS HTL, inhibits the interfacial reaction at the PEDOT:PSS/IT-4F interface. The suppression of the interfacial reaction at the PBDB-T-2F:IT-4F/HTL interface helps to retaining a stable and high V_0 across the BHJ, and thereby leading to a stable operation of the nonfullerene OSCs. Our findings highlight the importance of engineering robust device designs to mitigate any associated degradation pathways for attaining enhanced stability of NFA-based OSCs.

7. Experimental Section

Synthesis of MoO_3. The molybdenum (Mo) powders (Sigma-Aldrich) were used as received. 100 mg Mo powders were dissolved in 10 ml ethanol. Then the Mo power solution was stirred in the air for around 10 min. A 0.35 ml hydrogen peroxide (H_2O_2) solvent was then slowly dropped into the Mo solution. The reaction vessel was placed in an ice water bath to keep a constant reaction temperature for 20 h to form MoO_3 nanoparticles. The solution color gradually changed from greyish to grass green and then to dark blue MoO_3 nanoparticle solution with a concentration of around 0.1 mol/L. It was diluted 15 times with isopropyl alcohol (IPA) solvent before it was used for preparation of the HTL in OSCs.

Device Fabrication. ITO/glass substrates were cleaned by dilute detergent solution, deionized

water, acetone, and isopropanol for 20 min each and stored in the dry box before for device fabrication. HTL was spray coated on the top of ITO in air. The samples were transferred to the nitrogen-purged glove box with both O_2 and H_2O levels < 0.1 ppm for deposition of binary blend photoactive layer. The PBDB-T-2F:IT-4F/HTL/ITO/glass samples were annealed at 100 °C for 10 min before they were transferred to the vacuum chamber for top electrode deposition. The optimal weight ratio of PBDB-T-2F (Solarmer) to IT-4F (Solarmer) of 1:1 was used. Chlorobenzene (CB) together with 0.5% 1,8-diiodooctane (DIO) was used to form a solution with a concentration of 20 mg/ml. The solution was annealed at 25 °C and stirred at least 3 h before use. MoO_3 and PEDOT:PSS mixed solutions with different volume ratios of MoO_3 solution to PEDOT:PSS of 1:4, 1:3, 1:2, 1:1, 2:1, and 3:1 were used for preparing the MoO_3-PEDOT:PSS HTLs. Finally, the OSCs with an optimized structure of ITO/MoO_3-PEDOT:PSS (30 nm) /PBDB-T-2F:IT-4F (110 nm) /ZnO (20 nm)/Ag (100 nm) were fabricated. Control OSCs with a layer configuration of ITO/PEDOT:PSS (30 nm)/PBDB-T-2F:IT-4F (130 nm)/ZnO (20 nm)/Ag (100 nm) were fabricated. The OSCs were encapsulated to prevent the oxygen and moisture encroachment. The ratio of the IT-4F to PBDB-T-2F measured for the top surfaces of the binary blend layers was analyzed by measuring the elemental composition of the PBDB-T-2F:IT-4F layers deposited on the Si substrates. The ratio of the IT-4F to PBDB-T-2F at the bottom side of the blend films were also analyzed by removing the blend layer from the Si substrates by a transfer process using a polydimethylsiloxane mold. The removed PBDB-T-2F:IT-4F blend layers were then turned upside down (opposite to that deposited on Si substrates) prior to the XPS measurements.

Device Characterization

View Article Online
DOI: 10.1039/D0TA08018G

TPC measurement. A 532 nm Nd:YAG pulsed laser with a pulse duration of < 5 ns was used to generate the transient current in the OSCs. The OSCs were connected to an oscilloscope (Tektronix MDO3052 Mixed Domain Oscilloscope) for measuring the transient photovoltage. The function generator with a 50 Ω internal resistor was connected to cell in parallel for providing an off-set external bias. A laser pulse enters the OSCs from the ITO electrode side to generate the charge carriers. The photogenerated charge carriers drifted with V_0 to generate a transient photocurrent. The V_0 of the OSCs is estimated by applying an external bias to compensate the transient photocurrent in the TPC measurements.

Acknowledgements

This work was financially supported by the Research Grants Council of Hong Kong Special Administrative Region, China, General Research Fund (12302419), Collaborative Research Fund (C5037-18GF) and NSFC/RGC Joint Research Scheme (N_HKBU201/19).

References

1 Y. Cui, H. Yao, J. Zhang, K. Xian, T. Zhang, L. Hong, Y. Wang, Y. Xu, K. Ma, C. An, C. He, Z. Wei, F. Gao and J. Hou, *Adv. Mater.*, 2020, **32**, 1908205.

2 L. Zhan, S. Li, T. K. Lau, Y. Cui, X. Lu, M. Shi, C. Z. Li, H. Li, J. Hou and H. Chen, *Energy Environ. Sci.*, 2020, **13**, 635–645.

3 Z. Luo, R. Sun, C. Zhong, T. Liu, G. Zhang, Y. Zou, X. Jiao, J. Min and C. Yang, *Sci. China Chem.*, 2020, **63**, 361–369.

4 L. Meng, Y. Zhang, X. Wan, C. Li, X. Zhang, Y. Wang, X. Ke, Z. Xiao, L. Ding, R.

View Article Online
DOI: 10.1039/D0TA08018G

Xia, H. L. Yip, Y. Cao and Y. Chen, *Science (80-.).*, 2018, **361**, 1094–1098.

5 W. Li, L. Ye, S. Li, H. Yao, H. Ade and J. Hou, *Adv. Mater.*, 2018, **30**, 1707170.

6 Y. Lin, J. Wang, Z.-G. Zhang, H. Bai, Y. Li, D. Zhu and X. Zhan, *Adv. Mater.*, 2015, **27**, 1170–1174.

7 S. Holliday, R. S. Ashraf, A. Wadsworth, D. Baran, S. A. Yousaf, C. B. Nielsen, C. H. Tan, S. D. Dimitrov, Z. Shang, N. Gasparini, M. Alamoudi, F. Laquai, C. J. Brabec, A. Salleo, J. R. Durrant and I. McCulloch, *Nat. Commun.*, 2016, **7**, 11585.

8 H. Cha, J. Wu, A. Wadsworth, J. Nagitta, S. Limbu, S. Pont, Z. Li, J. Searle, M. F. Wyatt, D. Baran, J. S. Kim, I. McCulloch and J. R. Durrant, *Adv. Mater.*, 2017, **29**, 1701156.

9 D. Baran, N. Gasparini, A. Wadsworth, C. H. Tan, N. Wehbe, X. Song, Z. Hamid, W. Zhang, M. Neophytou, T. Kirchartz, C. J. Brabec, J. R. Durrant and I. McCulloch, *Nat. Commun.*, 2018, **9**, 2059.

10 T. Yan, W. Song, J. Huang, R. Peng, L. Huang and Z. Ge, *Adv. Mater.*, 2019, **31**, 1902210.

11 J. Yuan, Y. Zhang, L. Zhou, G. Zhang, H. L. Yip, T. K. Lau, X. Lu, C. Zhu, H. Peng, P. A. Johnson, M. Leclerc, Y. Cao, J. Ulanski, Y. Li and Y. Zou, *Joule*, 2019, **3**, 1140–1151.

12 B. Wu, Z. Wu, H. L. Tam and F. Zhu, *Appl. Phys. Lett.*, 2014, **105**, 103302.

13 Z. Wu, B. Wu, H. L. Tam and F. Zhu, *Org.Electron.*, 2016, **31**, 266–272.

14 B. Wu, Z. Wu, Q. Yang, F. Zhu, T. W. Ng, C. S. Lee, S. H. Cheung and S. K. So, *ACS Appl. Mater. Interfaces*, 2016, **8**, 14717–14724.

15 B. Xu, S. Gopalan, A. Gopalan, N. Muthuchamy, H. Jeong, J. Kwon, J. Bae and S. Kang, *Sci. Rep.*, 2017, **7**, 45079.

16 B. Xu, G. Sai-Anand, H. M. Jeong, S. W. Kim, J. S. Kim, J. B. Kwon and S. W. Kang, *Materials (Basel).*, 2018, **11**, 1143.

17 S. R. Dupont, E. Voroshazi, P. Heremans and R. H. Dauskardt, *Conf. Rec. IEEE Photovolt. Spec. Conf.*, 2012, 3259–3262.

18 K. Kawano, R. Pacios, D. Poplavskyy, J. Nelson, D. D. C. Bradley and J. R. Durrant, *Sol. Energy Mater. Sol. Cells*, 2006, **90**, 3520–3530.

19 A. Van Dijken, A. Perro, E. A. Meulenkamp and K. Brunner, 2003, **4**, 131–141.

20 X. Wang, C. Xinxin Zhao, G. Xu, Z. K. Chen and F. Zhu, *Sol. Energy Mater. Sol. Cells*, 2012, **104**, 1–6.

21 Y. Wang, W. Lan, N. Li, Z. Lan, Z. Li, J. Jia and F. Zhu, *Adv. Energy Mater.*, 2019, **9**, 1900157.

22 Y. Wang, B. Wu, Z. Wu, Z. Lan, Y. Li, M. Zhang and F. Zhu, *J. Phys. Chem. Lett.*, 2017, **8**, 5264–5271.

23 J. Han, Y. WANG and F. ZHU, *Energy Technol.*, , DOI:10.1002/ente.202000245.

24 W. Lan, Y. Wang, J. Singh and F. Zhu, *ACS Photonics*, 2018, **5**, 1144–1150.

25 M. H. Lee, L. Chen, N. Li and F. Zhu, *J. Mater. Chem. C*, 2017, **5**, 10555–10561.

26 S. Shao, J. Liu, J. Bergqvist, S. Shi, C. Veit, U. Würfel, Z. Xie and F. Zhang, *Adv. Energy Mater.*, 2013, **3**, 349–355.

27 S.Y. Chiam, B. Dasgupta, D. Soler, M.Y. Leung, H. Liu, Z.E. Ooi, L.M. Wong, C.Y. Jiang, K.L. Chang, J. Zhang, Solar Energy Materials & Solar Cells, 99 (2012) 197–

View Article Online
DOI: 10.1039/D0TA08018G

203.

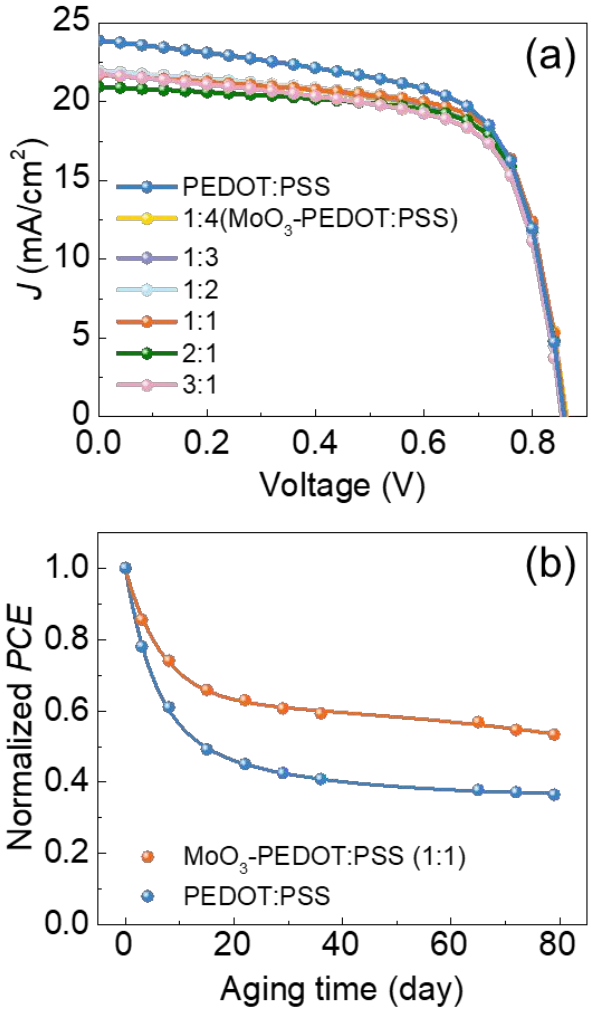

Figure 1. (a) *J–V* characteristics measured for the OSCs with a hybrid MoO_3-PEDOT:PSS HTL, prepared using having different volume ratios of MoO_3 solution to PEDOT:PSS. A pristine PEDOT:PSS HTL was used for the control cells. (b) Normalized *PCE* of the OSCs with a MoO_3-PEDOT:PSS HTL and the control cells as a function of the aging time.

View Article Online
DOI: 10.1039/D0TA08018G

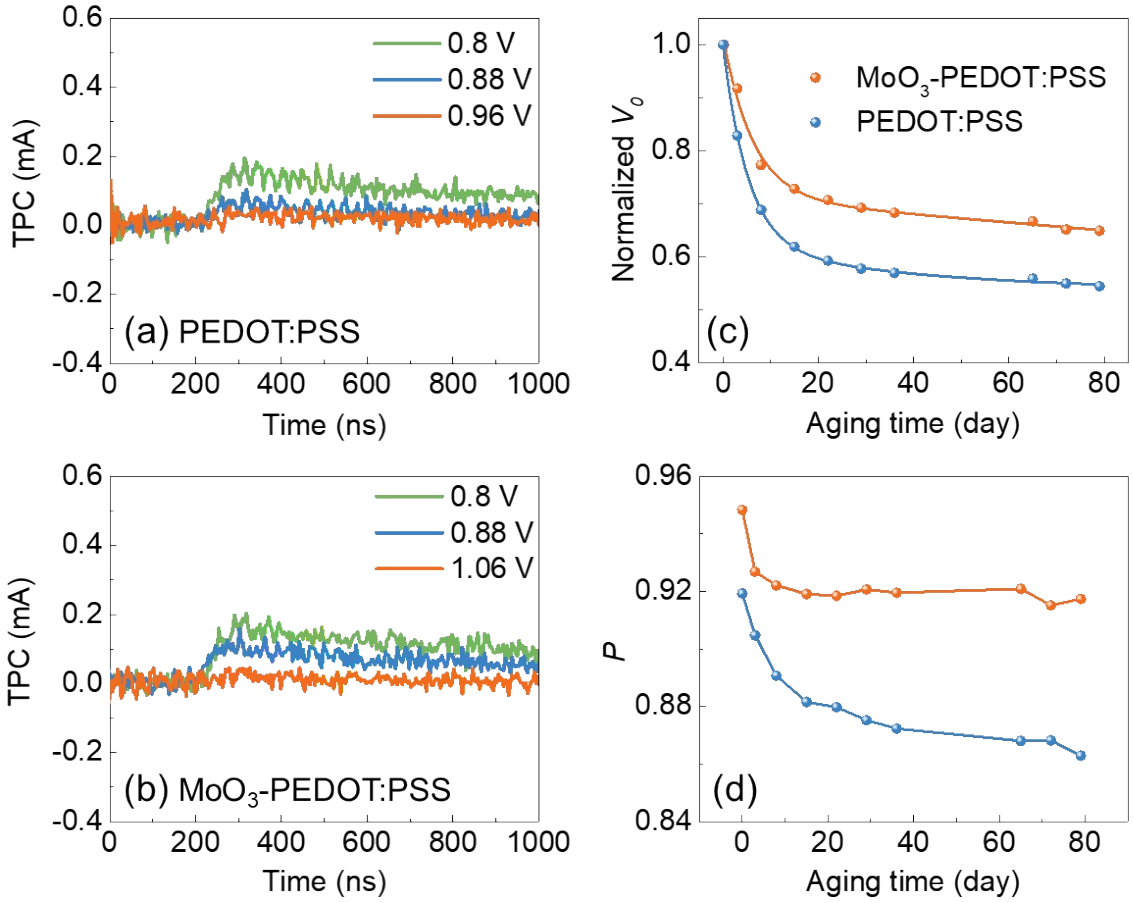

Figure 2. Transient photocurrents measured for the OSCs made with (a) a pristine PEDOT:PSS HTL and (b) a MoO_3-PEDOT:PSS HTL under different off-set biases. (c) The normalized V_0 and (d) the charge extraction probability as a function of the aging time, measured for an OSC with a MoO_3-PEDOT:PSS HTL and a control OSC.

View Article Online
DOI: 10.1039/D0TA08018G

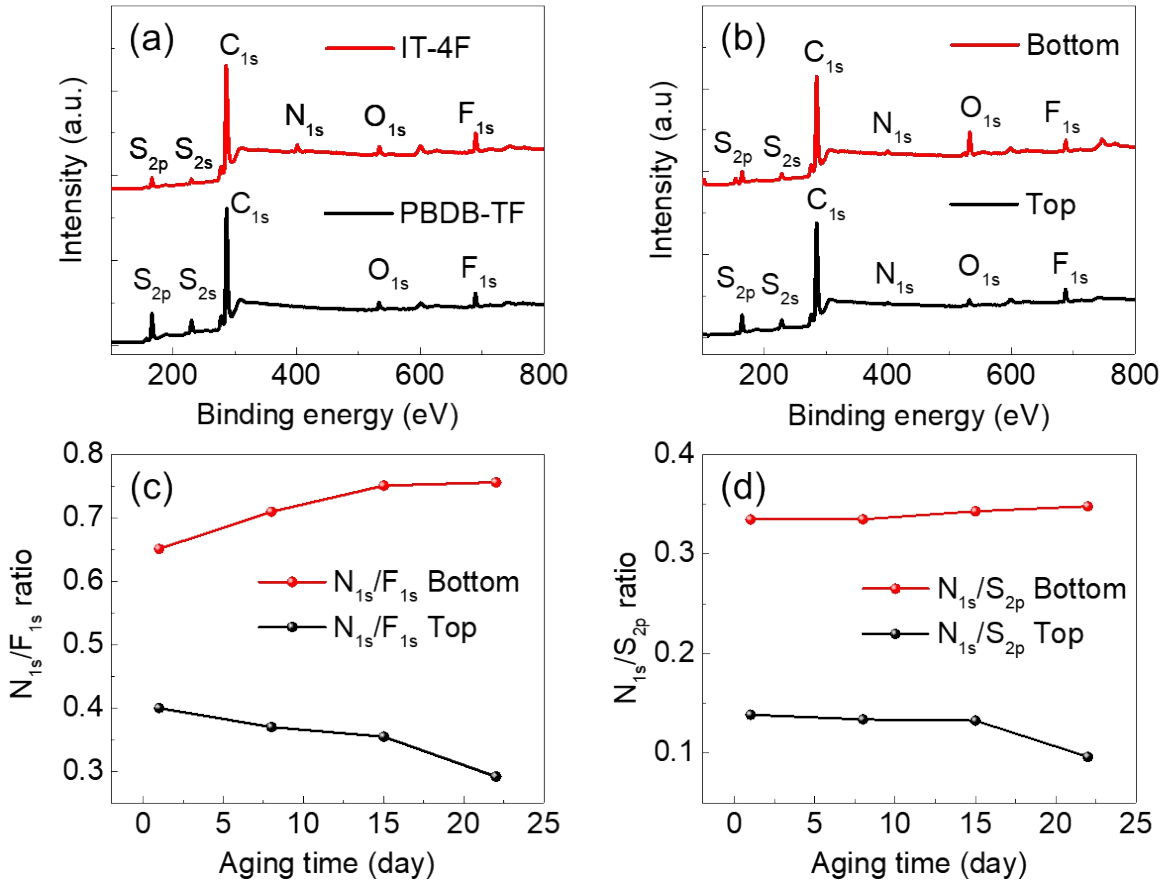

Figure 3. XPS scans measured for (a) a pure PBDB-T-2F layer and a pure IT-4F layer, and (b) the top and bottom surfaces of a PBDB-T-2F:IT-4F BHJ layer. (c) N_{1s}/F_{1s} and (d) N_{1s}/S_{2p} ratios at the top and bottom surfaces of BHJ as a function of the aging time.

View Article Online
DOI: 10.1039/D0TA08018G

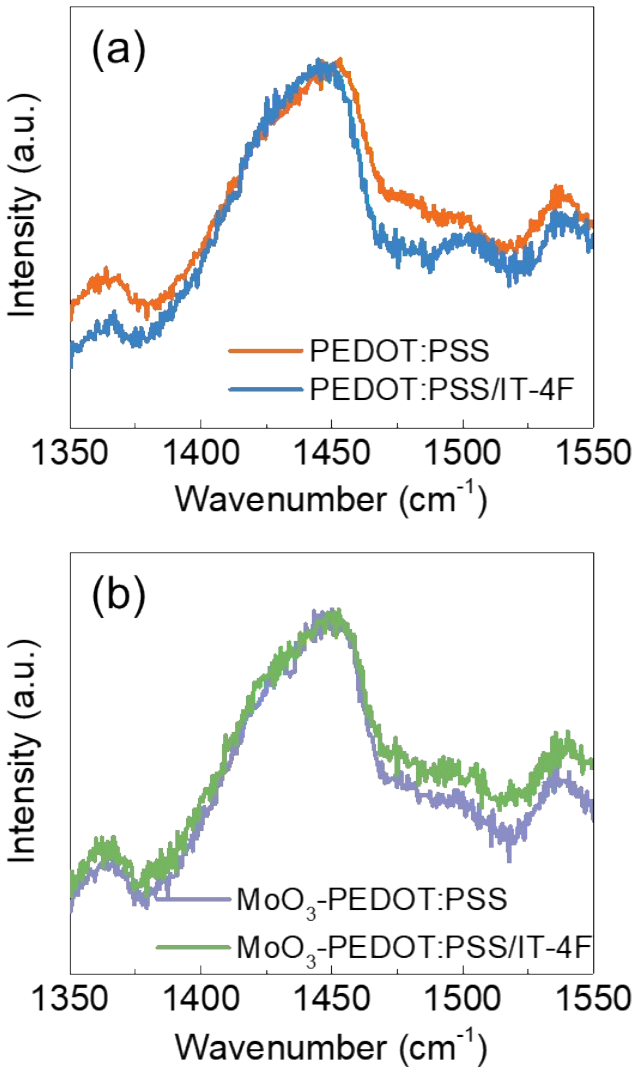

Figure 4. (a) Raman spectra measured for a pristine PEDOT:PSS film and an IT-4F film deposited on the PEDOT:PSS layer. (b) Raman spectra measured for a hybrid MoO_3-PEDOT:PSS film and an IT-4F film deposited on the hybrid MoO_3-PEDOT:PSS layer.

View Article Online
DOI: 10.1039/D0TA08018G

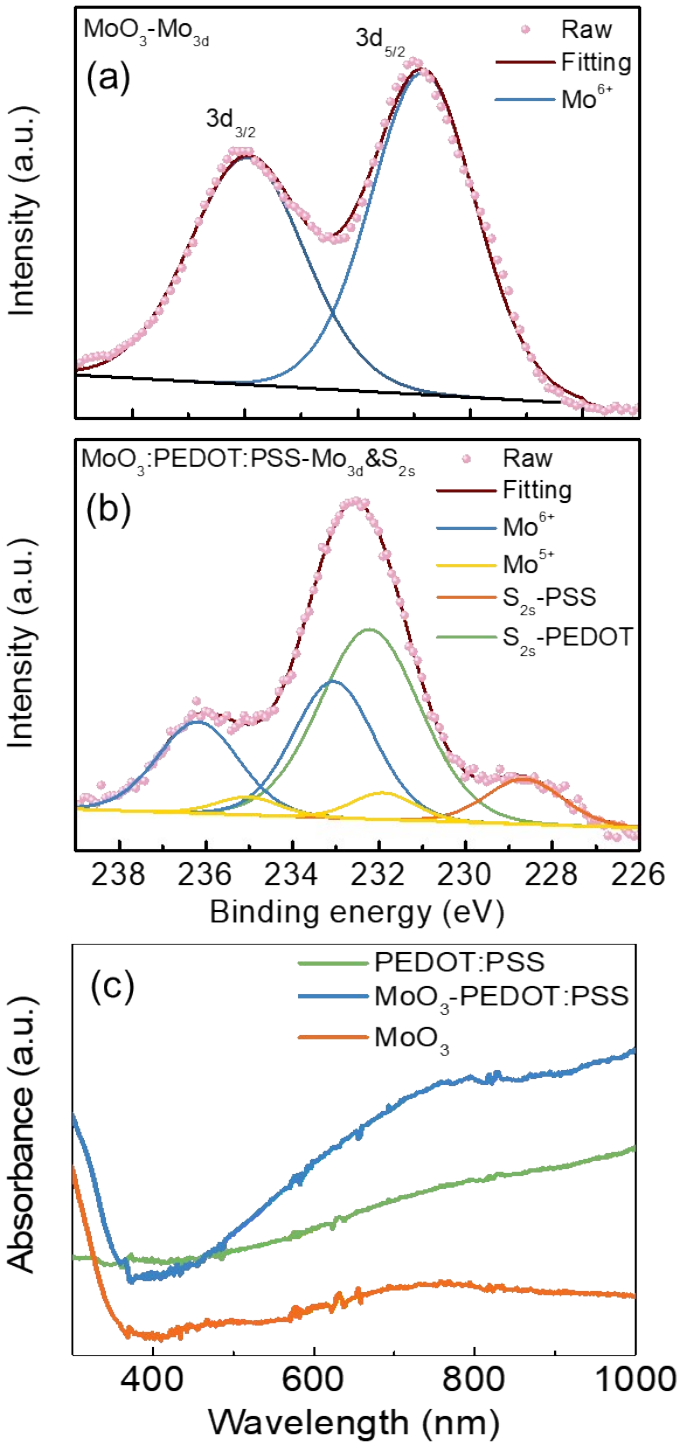

Figure 5. The Mo_{3d} XPS spectra measured for (a) a MoO_3 layer and (b) a MoO_3-PEDOT:PSS layer. (c) The UV-visible-NIR absorption spectra measured for a pristine PEDOT:PSS layer, a hybrid MoO_3-PEDOT:PSS layer and a pure MoO_3 layer deposited on the quartz substrates.

View Article Online
DOI: 10.1039/D0TA08018G

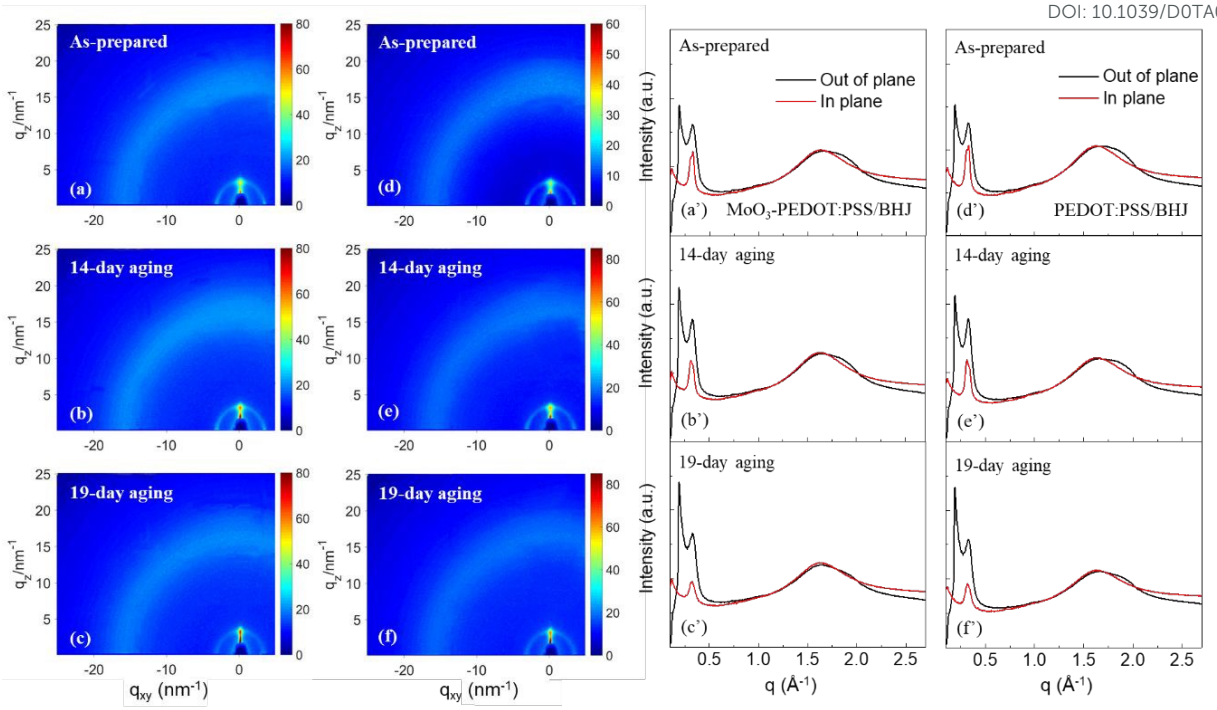

Figure 6. 2D GIWAXS patterns measured for the binary PBDB-T-2F:IT-4F blend layer deposited on the hybrid MoO_3-PEDOT:PSS HTL aged over different aging periods of (a), 0 day, (b) 14 days, and (c) 19 days). The corresponding 2D GIWAXS patterns measured for the binary PBDB-T-2F:IT-4F blend layer deposited on the pristine PEDOT:PSS film over different aging periods of (d) 0 day, (e) 14 days, and (f) 19 days. 1D line cuts in the in-plane and out of plane direction of the binary PBDB-T-2F:IT-4F blend layer on the top of the hybrid MoO_3-PEDOT:PSS film aged with different aging periods of (a'), 0 day, (b') 14 days, and (c') 19 days. 1D line cuts in the in-plane and out of plane direction of the binary PBDB-T-2F:IT-4F blend layer on the top of the pristine PEDOT:PSS film aged over different aging periods of (d') 0 day, (e') 14 days, and (f') 19 days.

DOI: 10.1039/D0TA08018G

Efficient and Stable Operation of Nonfullerene Organic Solar Cells: Retaining a High Built-in Potential

Yiwen Wang,[1] *Jiayin Han,*[1] *Linfeng Cai,*[1] *Ning Li,*[1] *Zhe Li**[2] *and Furong Zhu**[1]

[1] Department of Physics, Research Centre of Excellence for Organic Electronics and Institute of Advanced Materials, Hong Kong Baptist University, Kowloon Tong, Hong Kong, China
E-mail: frzhu@hkbu.edu.hk

[2] School of Engineering and Materials Science, Queen Mary University of London, London, United Kingdom
E-mail: zhe.li@qmul.ac.uk

The table of contents entry:

Modification of the hole transporting layer (HTL) helps to attain a high built-in potential across the bulk heterojunction (BHJ) through suppression of interfacial reaction at the HTL/BHJ interface. It is critical to retain a high and steady built-in potential to mitigate the associated degradation pathways, favoring the efficient and stable operation of nonfullerene OSCs.

ToC: